Case Studies in Thermal Engineering 3 (2014) 21–34

Contents lists available at ScienceDirect

Case Studies in Thermal Engineering

journal homepage: www.elsevier.com/locate/csite

An investigation of the effect of direct metal deposition parameters on the characteristics of the deposited layers

Tarak Amine [a,*], Joseph W. Newkirk [b], Frank Liou [a]

[a] Department of Mechanical and Aerospace Engineering, Missouri University of Science & Technology, United States
[b] Department of Metallurgical Engineering, Missouri University of Science & Technology, United States

ARTICLE INFO

Article history:
Received 25 November 2013
Received in revised form
23 February 2014
Accepted 23 February 2014
Available online 19 March 2014

Keywords:
Direct metal deposition
Microstructure
3D finite element modeling
Stainless steel 316L

ABSTRACT

Multilayer direct laser deposition (DLD) is a fabrication process through which parts are fabricated by creating a molten pool into which metal powder is injected as particles. During fabrication, complex thermal activity occurs in different regions of the build; for example, newly deposited layers will reheat previously deposited layers. The objective of this study was to provide insight into the thermal activity that occurs during the DLD process. This work focused on the effect of the laser parameters of newly deposited layers on the microstructure and mechanical properties of the previously deposited layers in order to characterize these effects to inform proper parameter selection in future DLD fabrication. Varying the parameters showed to produce different effects on the microstructure morphology and property values, leading to some tempering and aging of the steels. The microstructure of the top layer was equiaxed, while the near substrate region was fine dendritic. Typically, both the travel speed and laser power significantly affect the microstructure and hardness. Using the commercial ABAQUS/CAE software, a thermo-mechanical 3D finite element model was developed. This work presents a 3D heat transfer model that considers the continuous addition of powder particles in front of a moving laser beam using ABAQUS/CAE software. The model assumes the deposit geometry appropriate to each experimental condition and calculates the temperature distribution, cooling rates and re-melted layer depth, which can affect the final microstructure. Model simulations were qualitatively compared with experimental results acquired in situ using a *K*-type thermocouple.
© 2014 The Authors. Published by Elsevier Ltd. This is an open access article under the CC BY-NC-ND license (http://creativecommons.org/licenses/by-nc-nd/3.0/).

1. Introduction

In the direct laser deposition (DLD) process, the material in a single deposited layer typically is not enough to create a part. Several layers must be deposited to achieve a fully built part. With each newly deposited layer, the previously deposited layers begin to reheat, just one example of the multiple temperature gradients at play in the additive layering process that influence the material deposition.

The thermal behavior that occurs during the DLD process results in a complex microstructure evolution. Attributable to its stepwise additive nature, the thermal cycles associated with the DLD process can involve several reheating cycles. Thus, the goal of any assessment of microstructural evolution is to determine the response of the alloy to these cycles [1].

* Corresponding author. Tel.: +1 303 847 7381; fax: +1 573 341 4607.
E-mail address: taa89b@mail.mst.edu (T. Amine).

http://dx.doi.org/10.1016/j.csite.2014.02.002
2214-157X/© 2014 The Authors. Published by Elsevier Ltd. This is an open access article under the CC BY-NC-ND license (http://creativecommons.org/licenses/by-nc-nd/3.0/).

During the DLD process, the complex thermal distribution resulting from the repeated non-uniform heating and cooling process not only affects the mechanical performance and the post-machining precision of the fabricated component, but also results in fabricated component distortion, and possibly even cracking.

The microstructure of the material formed by the molten pool is related to the cooling rate during the solidification process. Further microstructural evolution takes place in the solid state depending on the subsequent temperature field and profiles developed within the samples as the laser is traversed during the build operation. Thus, it is important to control the temperature profiles during the DLD process so that an ideal microstructure can be achieved in the fabricated component. The most important DLD parameters include the laser power (W), travel speed (mm/min) and powder feed rate (g/min), which all significantly affect the microstructure of the formed parts [2].

The microstructure of DLD-fabricated materials clearly depends on the cooling rate and temperature gradient of the melt pool. Much research on the thermal behavior has concentrated on investigating the temperature distribution and cooling rate during the solidification process. However, the DLD process is more complicated than a series of successive solidifications of molten pools. During laser deposition, the previously deposited layers reheat when a new layer is deposited on top of them. The temperature of the sample varies from one location to another and from one point in time to another.

Ghosh (2006) developed a model to simulate the temperature distribution and residual stresses in the single-pass laser cladding process, which is very similar to DLD [3]. Giuliani (2009) developed a model to predict the powder temperature distribution for a laser with top-hat and Gaussian intensity distribution, as well as the temperature profile for a single-track laser [4]. Vahid et al. (2011) developed a model to simulate the shape and geometries of the real-time melt-pool and to predict the local solidification condition along the solid/liquid interface for a single-track laser [5]. However, it is important to understand and control the thermal behavior and reheating cycle attributed to building subsequent layers during the laser deposition process. So far, however, research on the effect of the reheating process that accompanies a multilayer build has been limited. In order to understand the evolution of and to control the microstructure, it is important to understand the thermal history of the deposited component during the DLD process, as was the focus of this work. Additionally, a transient thermal model of multi-thin wall multi-layers was developed to reveal the heating and reheating cycles during layer-by-layer deposition in the DLD process. The model was used to predict the temperature distribution, thermal gradient, re-melted layer depths, peak temperatures and cooling rate as a function of the DLD process parameters, such as laser travel speed (mm/min) and laser power (W).

The temperature history during the DLD process was measured by three thermocouples positioned to validate the model on the underneath surface of the substrate at the midpoint and ends of the laser track. The locations at which temperatures were measured were determined from finite element analysis (FEA) model; regions were selected in which the temperatures would not damage the thermocouples. These locations will be referred to as the reference positions for the measured temperatures. The thermocouples were connected via an interface box to a computer that monitored the temperatures at those positions during material deposition. The modeling results were qualitatively compared with experimental results acquired in situ using a *K*-type thermocouple. Moreover, the model ensures a constant molten pool temperature consistent with the number of deposited layers by reducing the laser power and increasing the laser travel speed as more layers are deposited.

2. Experimental procedure

The DLD system consists of the following components: 1 KW diode laser (coherent diode laser), a powder feeder and a 5-axis FADAL computer numerical control CNC (VMC3016) as shown in Fig. 1.

A computer-aided design (CAD) file and CNC control system were used to control the X, Y movement and Z increment. A series of thin walls were deposited with *K*-type thermocouples embedded at various points at schematic locations in the substrates. The temperatures were recorded with a data-logging system at a rate of 100 Hz per second. The data-logging system was initiated prior to the deposition and continued for several minutes after the deposition had finished. As a result, the entire thermal history of the reference positions during the deposition of the built part, including the cooling period after the deposition, was recorded.

The experiment was based on the three-level factorial design method to investigate the effects of three variables, the laser power (W), traverse speed (mm/min) and powder feed rate (g/min). The laser power and powder mass feed rate values were chosen on the basis of experience and previous experiments as being those required to grant values of specific energy and line mass close to the limits required for successful deposition.

The process parameter combinations used in the experiment appear in Table 1. In order to examine the influences of these parameters on the microstructure and properties of the deposited layers, the change of the microstructure of the side surface and the cross-sections of the deposited layers obtained at different laser powers and traveling speeds was observed and analyzed using scanning electron microscope (SEM). Subsequently, the mechanical properties, such as hardness, were examined at different positions of the deposited wall layers.

3. Material- stainless steel 316L

The substrate material serving as the deposition powder was 316L stainless steel, a common commercial alloy, $50 \times 50 \times 12.7\ mm^3$ in length, width and height, respectively. The chemical composition range of 316L stainless steel appears in Table 2. The offset between the laser head and deposition point was a constant 5 mm.

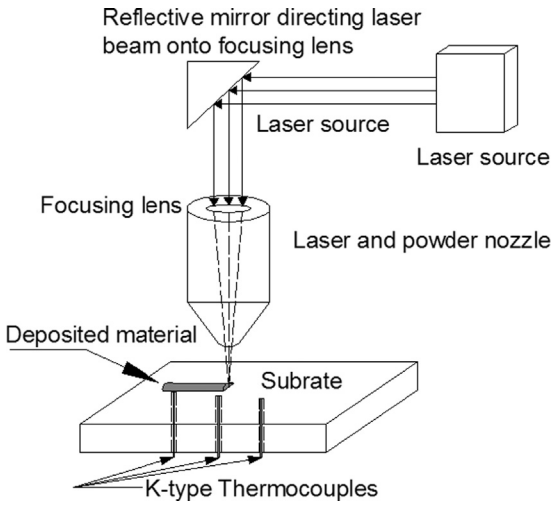

Fig. 1. Schematics of a direct laser deposition process system.

Table 1
Process conditions monitored.

Sample #	Laser power (W)	Traveling speed (mm/min)	Powder feed rate (g/min)
1	600	300	8
2	600	375	10
3	600	450	12
4	750	300	10
5	750	375	12
6	750	450	8
7	900	300	12
8	900	375	8
9	900	450	10

Table 2
Chemical composition range of 316L stainless steel.

Element	C	Mn	P	S	Si	Ni	Cr	Mo	Fe
(Wt%)	<0.03	<2	<0.045	<0.03	<1	10–14	16–18.5	2–3	Bal.

4. Thermocouple measurements

Controlling the thermal behavior to reproducibly fabricate parts is important. To monitor the heat gradient of both the laser track and the reheating process caused by the subsequent layers in order to determine the evolution of unique microstructural features in multilayer builds, a new scheme was designed for locating thermocouples on the substrate. *K*-type thermocouples were attached on the underneath surface of the substrate at the midpoint and ends of the laser track. The thermocouples were connected via an interface box to a computer that monitored temperatures at those positions throughout the deposition process.

5. Thermal modeling

Fig. 2 depicts a flow chart showing various steps in the computational scheme employed in the study. The entire deposition process was modeled as a multistep transient heat transfer analysis in which each time step was further divided into a number of smaller time increments. The continuous addition of metal powders was considered by means of the successive, discrete addition of a new set of elements into the computational domain at the beginning of each time step, which was fixed such that the laser beam scanned the distance equal to a set of newly activated elements.

The number of elements activated at each time step was determined from the volume of powder materials expected to enter the melt pool during that time step, which depended on the powder feed rate (f) and the travel speed of the laser (v).

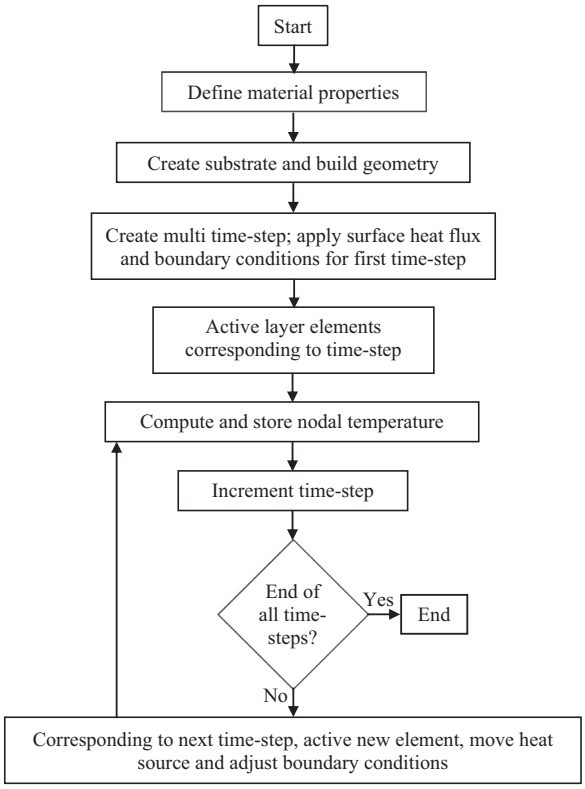

Fig. 2. Flow chart showing various steps involved in the temperature distribution model.

Table 3
Thermal material properties for stainless steel 316L as used in the finite element modeling.

Temperature (K)	300	400	500	600	700	800	1000
Specific heat (kJ/kg K)	468	504	527	550	563	576	602
Expansion coefficient alpha (m/mK)	1.52E−5	1.61E−5	1.69E−5	1.75E−5	1.79E−5	1.83E−5	1.88E−5
Conductivity (W/mK)	13.4	15.2	16.75	18.3	19.8	21.3	24.2

A 3D finite element temperature field model for DLD developed using ABAQUS/CAE software demonstrated the model's thermal history in stainless steel SS316L. Transient thermal analysis first was performed within ABAQUS/CAE to determine the temperature history at each reference position in the deposited material. Eq. (1) is the heat conduction governing equation:

$$d/dx(KdT/dx)+d/dy(KdT/dy)+d/dz(KdT/dz)=\rho C_p dT/dt \tag{1}$$

where ρ, C_p, and K refer to the density, specific heat, and thermal conductivity, respectively, of the metal powder and the substrate material; and T and t represent the temperature and time variables, respectively. The terms on the left side of Eq. (1) refer to the conductivity heat transfer in the x, y, and z directions, respectively. The terms on the right side of Eq. (1) refer to the transient nature of the heat transfer process.

The first step began with a substrate material, T_0, initially at room temperature, as shown in Eq. (2). At the beginning of each subsequent step, a new group of finite elements was activated.

$$T(x,y,z)=T_0 \tag{2}$$

Given the melt generation and resolidification associated with phase change effects, the specific material properties used as inputs in the current analysis were density, thermal conductivity (K), specific heat, enthalpy (H) and latent heat for varying temperature ranges. Numerical values of these material properties as adopted from [6] and used in the analysis appear in Table 3. All substrate surfaces exposed to the environment were assumed to have lost heat due to free convection.

In order to simulate mass addition (powder deposition), the “birth and death” feature in ABAQUS/CAE was used. Initially, all elements in the deposited track were “killed”. The total time required for the laser beam to travel along the deposited track of each layer was divided into a number of small time steps to which variable flux and boundary conditions were

applied. The first born of the element set appeared with applying these conditions. For the subsequent element sets, the model used the results of the previous step as the initial condition for the new active element set.

Finally, according to Rosenthal's Eq. (3), the moving heat source was simulated by applying a concentrated surface heat flux on the model for a time equal to the distance between the model element sets divided by the laser travel speed. A user subroutine was written to calculate the position of the laser at a given time as a function of its speed (v) and the Gaussian flux distribution in terms of spatial coordinates.

$$\rho C_p dT/dt - \rho C_p \nabla(vT) - (K\nabla T) = Q \tag{3}$$

where T is the temperature and Q is the power generation per unit volume of the material.

As assumed in the simulation, the interaction of the heat flux with both the substrate and the deposited material follows the schematic in Fig. 4, such that at time t during beam scanning, the heat flux as the source of heat from the laser beam was modeled at the location Lt on the surface of the substrate along the path of scanning. This simulated the impinging beam onto this surface at that instant, resulting in the generation of a melt pool. The deposit was the solidified form of powder particles added into the melt pool, so it was modeled on top of the heat source to simulate the volume of added powder particles. As the beam moved to a new location after a time $t+dt$, the heat flux correspondingly moved to the location Lt$+dt$, with $v\,dt$ being the length of deposited material over the incremental time dt. The analysis was divided into several steps in order to move the heat flux from the laser over the nodes in the laser path.

5.1. Geometric model of the thin wall

In order to predict the temperature distribution of the deposited thin wall in the DLD process, 3D finite element and meshes were built using Hypermesh software, as shown in Fig. 3. The mesh on the geometry, which represents its discretization into the elemental form, is made of thermal 8-node linear brick type elements. It was generated such that the wall region, where fusion occurs and more severe temperature gradients are expected, was assigned the finest mesh, and regions further from the wall were assigned a relatively coarse mesh [7–10]. The DLD process was simulated using ABAQUS/CAE.

5.2. Case study

The structure of the deposited thin wall in the model was built by depositing multi-layer and single-layer tracks on top of each other with a length of 30 mm, height of 14 mm, and width of 2.5 mm. The wall was fabricated on a surface of 316L

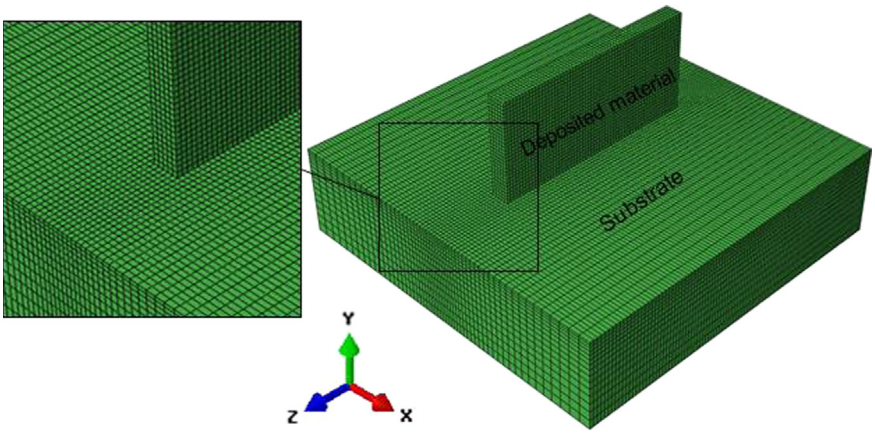

Fig. 3. 3D finite element model build and meshes using Hypermesh.

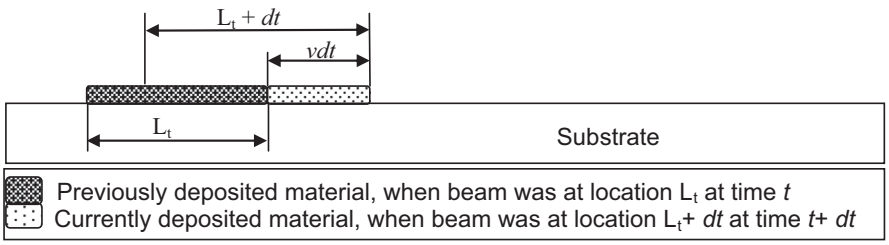

Fig. 4. Schematic illustration of beam/substrate interaction at different times during beam scanning, and length of clad, vdt, which is manufactured in every scan over a time of dt.

stainless steel that was 50 mm wide, 50 mm long and 12.7 mm thick, as shown in Fig. 3. To simulate the laser deposition process, the following assumptions were made:

- The initial temperature of the workpiece was assumed as 295 K. The workpiece and the coordinate mesh were fixed. The laser beam was moved in both the positive and negative z-direction with a constant speed v. For newly deposited layers, the laser beam was moved up in the positive y-direction.
- A subroutine was written to consider the effect of conduction, convection and radiation during the laser deposition process.
- The following boundary conditions were applied to the deposited thin wall

$$q = -h(T-T_0)$$

$$q = \sigma \in (T^4-T_0^4)$$

where q is the heat flux per unit area, h is the convective heat transfer coefficient, $\in$ is emissivity, σ is the Stephan–Boltzmann constant and T_0 is the ambient temperature.

- The thermo-physical properties of 316L stainless steel were considered as function of the temperature, as illustrated in Table 1.
- A radiation boundary condition was applied to the entire deposited thin wall, and the emissivity was assigned a value of 0.4.

The thin walls were built using a 1 kW diode laser, a multiaxis numerical control working table, and a powder feeder with a coaxial nozzle.

The thermal load, applied as a function of the distance, was determined using Eq. (4)

$$\mathrm{DFLUX}(1) = q(0)e - cr^2 \tag{4}$$

where $r = x^2 + y^2 + z_1{}^2$, $z_1 = z - v(T-t)$, v is the speed of movement in the z-direction, T is the lag factor that defines the first position of the laser gun, t is time, z_1 is movement along the z-axis, and z is a fixed coordinate axis.

6. Results and analysis

The influence of the laser parameters on the shape and size of the laser melting pool was evaluated by specifying the actual power (P), travel speed (v) and beam diameter (D_b) as the specific energy (E_s) by means of Eq. (5).

$$E_s = P/(D_b v) \tag{5}$$

6.1. Microstructure

The microstructure plays a crucial role in determining the properties of a component. In this study, the optical and scanning electron micrographs of the top surface and cross-section of the laser-assisted fabricated layer were observed in detail to study the morphology and grain size, as well as how these were affected by the laser parameters.

Fig. 5 shows the SEM micrographs of different positions of the laser deposition zone prepared with an actual power of 600 W, laser travel speed of 300 mm/min and beam diameter of 5 mm. Whenever the laser power increased, the dendritic structures of the deposited material gradually altered from thin to coarse, which means that the primary dendritic spacing was augmented as the dendrite grew.

As the laser travel speed increased, the microstructural composition of the deposited layer changed from coarse dendrites to fine dendrites. This change was attributed to a decrease in the ratio of the temperature gradient to the solidification rate, which can be estimated using Eq. (6) [11]

$$G/R = 2\pi K(T-T_0)^2/\eta P v \cos\theta \tag{6}$$

where G is the temperature gradient, R is the solidification rate, v is the laser traveling speed, T is the temperature of the liquid, T_0 is the preheated temperature of the substrate, η is the laser absorption coefficient, P is the laser power and K is the thermal conductivity of the material.

A homogenous, defect-free, 316L stainless steel deposited microstructure was obtained. Fig. 6 shows the homogenous cellular appearance of the microstructure at the cross-section after the direct laser deposition of 316L stainless steel using the defined conditions. The deposition was free of cracks, and the microstructure was mostly cellular, with grain sizes ranging from approximately 15 to 35 μm. The highest microhardness value was associated with a homogenous microstructure and the smallest grain size.

The microstructure of the deposited material has been shown to depend highly on the laser deposition process parameters. Under a narrow range of parameters, a defect-free, homogenous microstructure can be obtained [12,13].

In the process of rapid directional solidification with an ultra-high temperature gradient, it is beneficial to obtain an ultrafine microstructure, which results in a more uniform distribution of the components and higher strength. The microstructure that forms in DLD parts is dependent on the cooling rate of each layer from the peak temperature at a certain

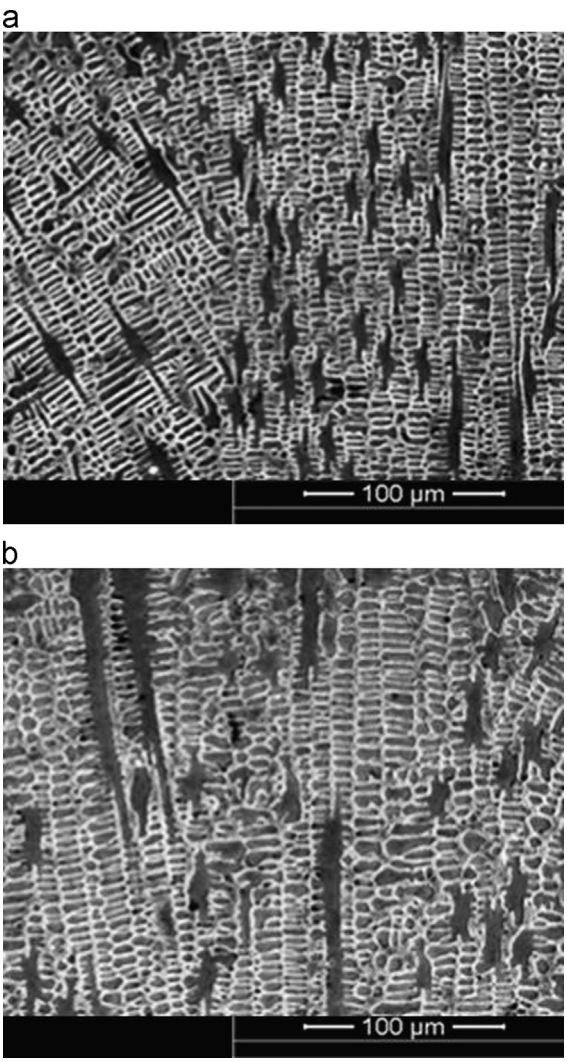

Fig. 5. Microstructure at 600 W, 300 mm/min in different positions of the laser deposition zone: (a) top layers and (b) bottom layers.

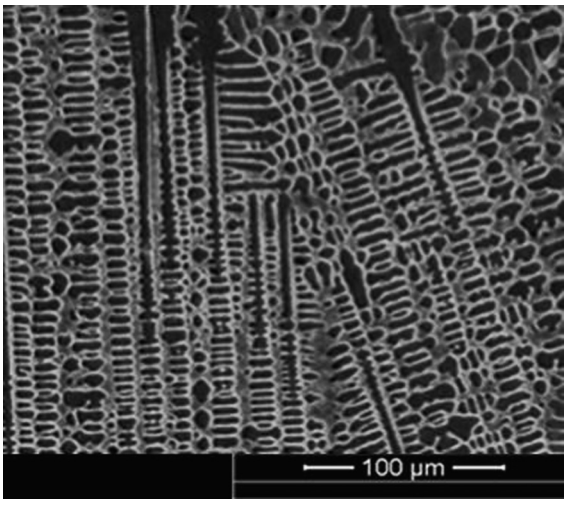

Fig. 6. Appearance of homogenous cellular microstructure of laser-deposited stainless steel 316L600, 450 mm/min.

point in the peak temperature period. Slow cooling rates result from conditions of high incident energy (high power setting and low travel speed), while fast cooling rates result from low laser power and high laser travel speed.

6.2. Microhardness analysis

Microhardness measurements were made on a cross section of both the substrate and deposited material, beginning at the substrate moving toward the deposited material. The microhardness analysis of the deposited specimens showed that the average microhardness varied from 185 to 280 HV across all samples. Hardness variations were observed in both the deposited and heat affected zones. Increased hardness was attributed to the process parameters [14].

The microhardness profiles of 316L stainless steel samples subjected to the investigated laser parameters are illustrated in Fig. 7a and b. Microhardness measurements were taken at increments of 1000 μm for the deposited region and 500 μm for the substrate.

The effect of the laser parameters on the hardness of the deposited material and heat affected zone are summarized in Fig. 8. The hardness values reported in the figures are the average values of the hardness measured in the deposited material and heat affected zone.

In general, the hardness of the deposited material decreased as the laser power increased and as deposition progressed toward the top layers. On the other hand, the hardness of the heat affected zone increased with the laser power. At a constant laser power, the hardness of both the deposited material and the heat affected zone decreased as the travel speed of the laser beam increased.

The rapid heating and cooling cycles associated with the laser deposition process increase the thermal stress and, as a result, the dislocation density. The most important factor in determining the grain size and thus the hardness is the cooling rate. Increasing the cooling rate during solidification could produce deposited material with finer grains. Other important effects occur when using high laser power, which lowers the cooling rate, thereby forming coarse dendrites that reduce the hardness.

Results published in [15] literature showed reduced thermal activity as the energy source moves away from a substrate during deposition. At the beginning of material deposition, the heat quickly dissipated via the heat conduction of the substrate. This initial thermal transience produced a rapid quenching rate effect at the beginning stage of the laser deposition process, which resulted in increased hardness.

In the heat affected zone, the hardness varied according to the location at which it was measured. The region close to the deposited material had higher hardness values than regions far away from the deposited material.

Increases in hardness were observed as the travel speed at a constant laser power increased. This effect was caused mainly by the limited interaction between the laser and the powder; only a low amount of energy was supplied during the melting process. This low energy limited the amount of time available for growth, therefore increasing the hardness.

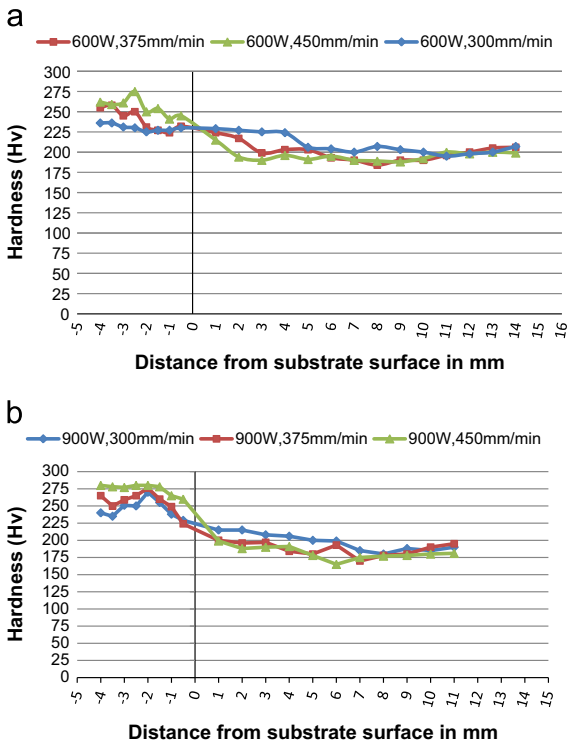

Fig. 7. Microhardness profile at 300, 375 and 450 mm/min: (a) 600 W, (b) 900 W.

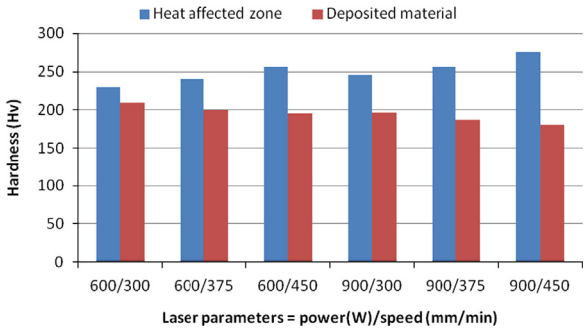

Fig. 8. The effect of laser parameters on the hardness of deposited material and heat affected zone.

6.3. Grain size

In general, the cooling rates experienced by laser-deposited 316L stainless steel samples decreased as the distance from the substrate increased due to the increased heat and the build-up of mass during deposition.

Observed from the side, the surfaces of the components exhibited a layered structure from the laser deposition and showed large, elongated grains. These grains grew epitaxially, inclined in a direction toward the layers following the temperature field resulting from the moving laser torch.

The grain size decreased as the traverse speed increased, as shown in Fig. 9a and b, but was largely affected by the power level. Thus, the grain size also tended to increase with incident energy (=laser power/laser traverse speed), as seen in Fig. 9c. This trend was expected because grain size tends to decrease as the cooling rate increases. High energy results from a combination of high power and low travel speed, yielding a low cooling rate. Conversely, low energy results from a combination of low power and high travel speed, yielding a high cooling rate [16].

The secondary dendrite arm spacing was measured and is illustrated in Fig. 10a, b and c. The relationship between the hardness of the 316L stainless steel and the secondary dendrite arm spacing is plotted in Fig. 11. The curve clearly indicates that the hardness of the 316L stainless steel increased as the secondary dendrite arm spacing decreased. The hardness of the 316L stainless steel was correlated with the secondary dendrite arm spacing (d) using the straight line Eq. (7):

$$H = Ad + B \tag{7}$$

where A and B are constants.

The secondary dendrite arm spacing cell size was determined using Eq. (8):

$$d = (d_1 + d_2)/2 \tag{8}$$

where d_1 is the length of a secondary arm, and d_2 is the approximate diameter.

In this work, the secondary dendrite arm spacing of the 316L stainless steel decreased as the cooling rate increased. As the cooling rate decreased, there was enough time for the small dendrite arms to melt and disappear, which occurred as a result of their high surface area to volume ratio increasing their total energy per unit volume. As the small dendrite arms disappeared, the secondary dendrite arm spacing of the alloys increased [2].

The secondary dendrite arm spacing of the 316L stainless steel decreased as the cooling rate increased during solidification. As the secondary dendrite arm spacing decreased, the hardness of the 316L stainless steel increased.

6.4. Thermocouple measurement

Regarding the thermal histories within the deposited material during deposition, Fig. 12 shows the temperature variation of the underneath surface of the first deposited layer at the right end (T_1), middle (T_2) and left end (T_3) of the deposited wall with depths of 1, 2, and 3 mm, respectively, which directly impinged on the substrate, while the subsequent 87 layers were deposited in sequence with parallel deposition.

Oscillations were the most obvious characteristic of the temperature measurements. Each temperature peak represented the thermocouple's response as the laser passed over it. The temperature increased when more and more energy was transferred to this position by heat conduction. The thermal excursion decayed when either the energy source moved away from the thermocouple during the deposition of a layer or when subsequent layers were deposited. The thermocouples were attached on the substrate, so the measured temperatures were much lower than those near the molten pool.

6.5. Simulation analysis

Fig. 13 illustrates the transient temperature distribution contour plot for the first deposited layer for the case of Q=600 W and V=300 mm/min. The location of the laser beam is evident from the intensity of the temperature distribution,

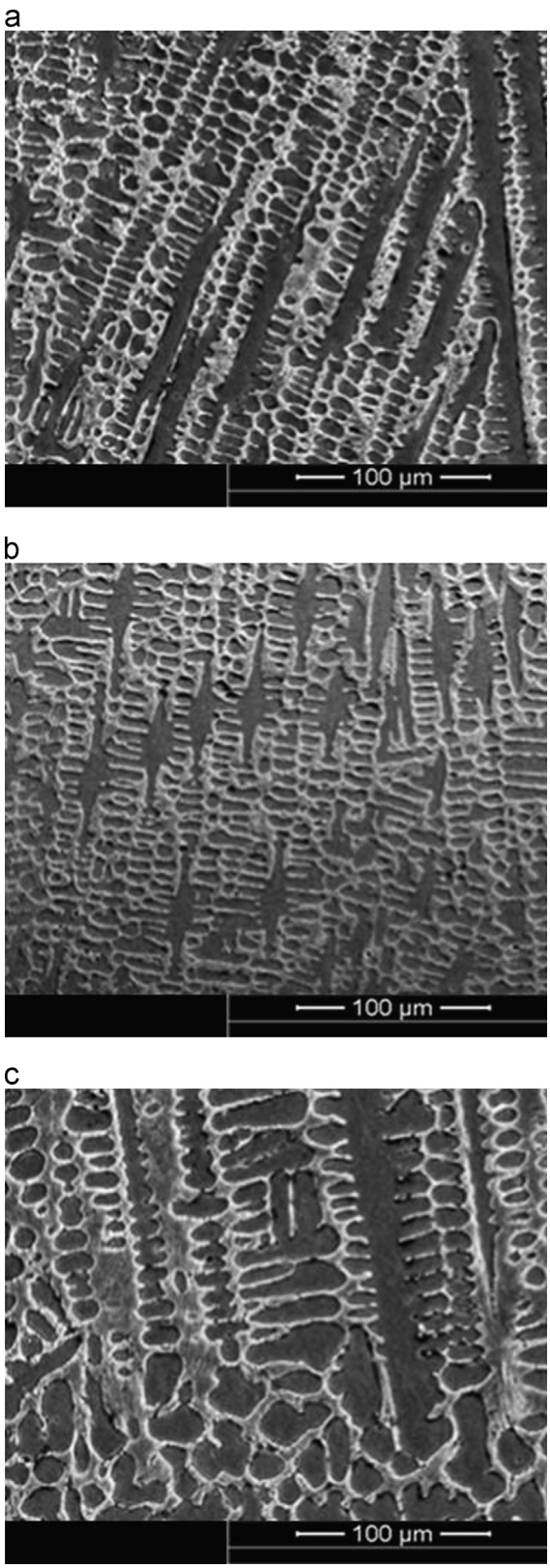

Fig. 9. Microstructure at (a) 750 W, 300 mm/min, (b) 750 W, 450 mm/min, and (c) 900 W, 300 mm/min.

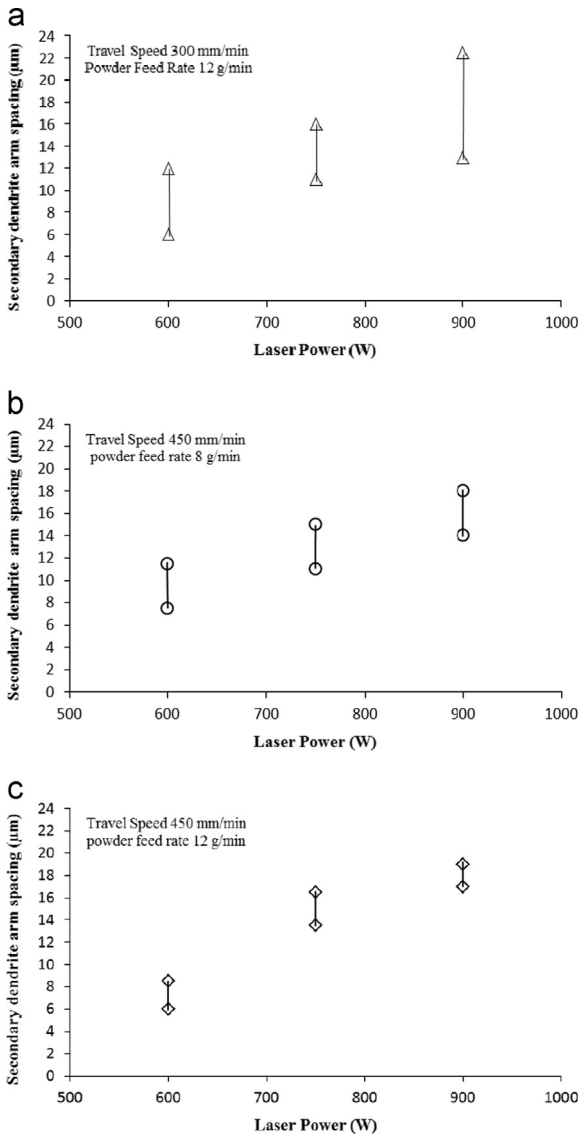

Fig. 10. Range of secondary dendrite arm spacing (d) as a function of applied laser power for DLD of 316L stainless steel.

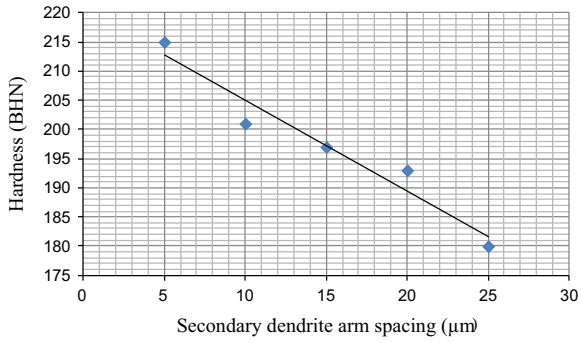

Fig. 11. Curve showing the effect of secondary dendrite arm spacing (d) on the hardness of the 316L stainless steel.

where the maximum contour limit of 1996 °C signifies the melt pool. The thermal history was essentially independent of the vertical free edges once the laser reached the center of the wall, where the mesh was highly refined, as shown in Fig. 3, for accurate extraction of the thermal gradient and cooling rate.

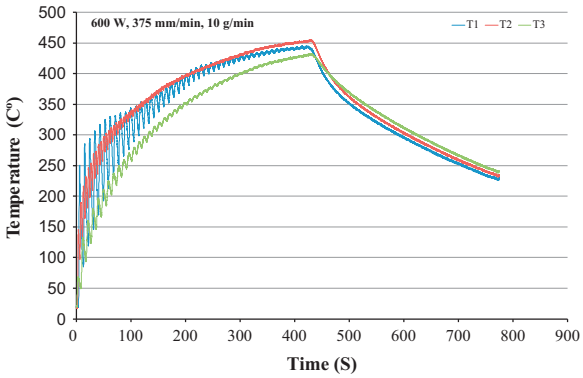

Fig. 12. Thermal history at the underneath surface of the first deposited layer, while 87 subsequent layers are deposited.

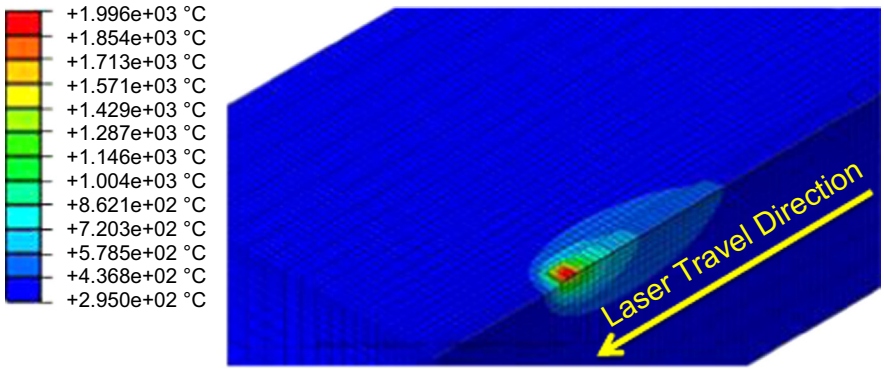

Fig. 13. Temperature contours for $Q=600$ W and $V=300$ mm/min.

Fig. 14a and b illustrates the temperature distribution along the deposited layers and substrate simulated using the defined laser parameters. The temperature of each nodal point within the solid was calculated as a function of time. The bottom of the deposited layers cooled faster than the top because of heat conduction to the substrate, while showing significant temperature gradients along the height of the deposited layers.

Thermal energy from the laser increased the node temperature beyond the melting temperature. Once the laser moved away along its track, the node began to cool. The next pass of the laser caused the temperature of that node to increase higher than during the previous laser pass.

As seen in Fig. 14a and b, the numerical results are similar to the experimental results. The simulated results for different values of absorptivity were compared with the experimental results, and a maximum error of approximately 20% was observed in the simulated results for absorptivity of 0.6. The uncertainty in the measurement was approximately 100 °C, which could have been slightly higher because the thermocouple beads were exposed to some laser energy by radiation. Also, a slight phase shift is apparent between the graphs of the simulated and experimental results. This difference eventually disappeared during cooling. This shift could have been due partially to the acceleration/deceleration of the laser; additionally, the dwell times while changing laser tracks between layers was not considered in the model [9].

In order to achieve a uniform thickness of a thin deposited wall and to keep the molten pool temperature constant in accordance with the number of laser-deposited layers, the laser power was reduced, and the laser travel speed was increased continuously with the number of deposited layers due to less heat sunk through the workpiece.

The cooling rate of the FEA model was extracted from the time difference between when the nodes in the center of the deposited material were seen at the last liquids temperature and at the next solidus temperature. At each nodal location, the solidification cooling rate was determined using

$$dT/dt = |T_l - T_s|/|t_l - t_s| \tag{9}$$

where dT/dt is the cooling rate, $T_l - T_s$ is the difference between the liquids and solids temperatures, and $t_l - t_s$ is the time interval between T_l and T_s.

The computed results of the FEA model showed that the cooling rate of the thin wall was affected by the number of deposited layers. The cooling rate was high at the beginning of the deposition process in the first and second layers because the heat transferred to the substrate, but then it decreased with the addition of subsequent layers. The predicted cooling rates ranged from 200 °C/s to 5500 °C/s.

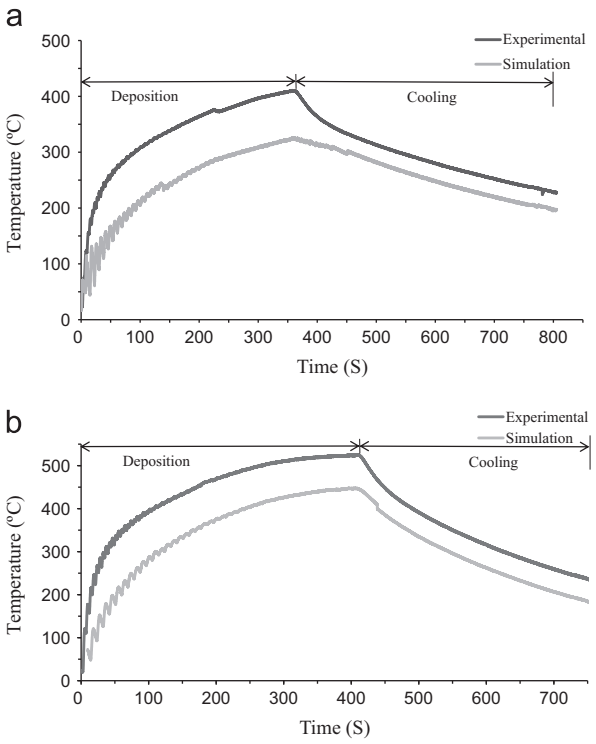

Fig. 14. Comparison of simulation and experimental results predicted at different reference positions: (a) 600 W, 450 mm/min, 12 g/min and (b) 900 W, 375 mm/min, 8 g/min.

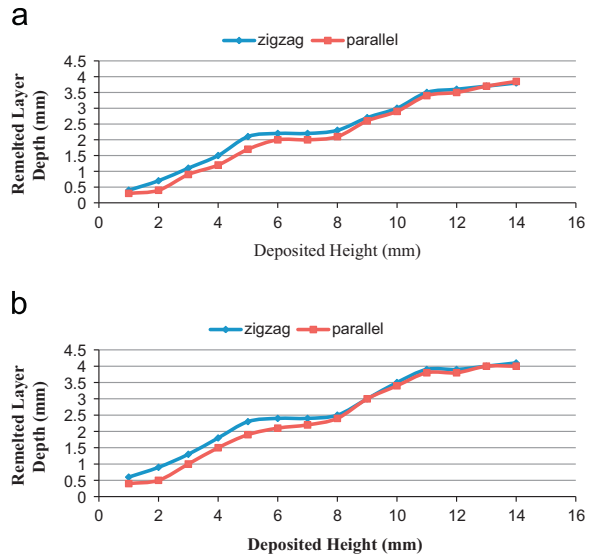

Fig. 15. Computed remelted layer depth at (a) 600 W 300 mm/min and (b) 900 W 300 mm/min.

The model was also used to predict the re-melting depth during laser deposition, an important factor to consider. The frequent re-melting of previous layers can lead to unwanted precipitation of phases or solutes, which can become detrimental metallurgically. Fig. 15a and b shows the simulated re-melted layer depths of deposited layers. These results were extracted from the simulation when the solidified node re-melted ($T > T_m$) each time the laser beam passed over it. In general, the depths of the re-melted layers were high, except for in the first layer, which bounded on the substrate and had difficulty melting completely because of the heat sinking to the substrate via heat conduction.

Fig. 15a and b illustrates that the re-melted depth accompanying the parallel laser scanning path was lower than that accompanying the zigzag path during the early stage of deposition because of the slightly higher cooling rate, though this

effect eventually disappeared. Also, a lower laser power resulted in fewer re-melted layers as a result of the higher cooling rate of the build wall.

Increasing the laser travel speed and/or decreasing the laser power reduced the melt pool depth. All of these extracted results provide important metallurgical information.

7. Conclusion

The temperature field evolution, thermal cycling characteristics, temperature gradient and effects of different deposition directions on the thermal activity of single-pass, multi-layer laser deposition fabrication were investigated.

In general, the traveling speed and laser power were shown to significantly affect the microstructure.

The DLD process in the same deposition direction exhibited larger temperature gradients than in the reverse deposition direction, and heat diffusion in the same deposition direction was better.

The thermal behavior associated with the DLD process involves numerous reheating cycles. As a result, the temperature history of the deposited materials can be considered as a series of discrete pulses.

A 3D transient thermo-mechanical finite element model with a moving laser beam was developed to predict the temperature at any location and time during the laser deposition process. Element removal and reactivation technology were used in the modeling to realize the stepwise pattern of material addition.

The FEA model revealed the significant effects of the processing parameters, such as the laser power and travel speed. The results showed that increasing the laser power and/or decreasing the laser travel speed markedly increased the peak temperatures, cooling rates and dimensions of the melt pool.

A *K*-type thermocouple was used to measure the temperature history of multiple layers of deposited material. The measurements were qualitatively compared with the prediction of the 3D transient thermo-mechanical finite element model.

References

[1] Kell J, Tyrer JR, Higginson RL, Thomson RC. Microstructural characterization of autogenous laser welds on 316L stainless steel using EBSD and EDS. J Microsc 2005;217:167–73.
[2] Qin Y, Qin Yi, Juster Neal P. Advances in manufacturing technology XVII, 1st Edition; 2003. p. 132.
[3] Ghosh S, Choi J. Modeling and experimental verification of transient/residual stresses and microstructure formation in multi-layer laser aided DMD process. Heat Transfer Div ASME 2006;128.
[4] Giuliani Valerio, Hugo Ronaldo, Gu Peihua. Powder particle temperature distribution in laser deposition technologies. Rapid Prototyping J 2009;15/4:244–54.
[5] Fallah Vahid, Alimardani Masoud, Corbin Stephen, Khajepour Amir. Temporal development of melt-pool morphology and clad geometry in laser powder deposition. Comput Mater Sci 2011;50:2124–34.
[6] Goodfellow. Metals, alloys, compounds, ceramics, polymers, composites. Catalogue 1993/94.
[7] Abid M, Siddique M. Numerical simulation to study the effect of tack welds and root gap on welding deformations and residual stresses of a pipe-flange joint. Int J Pressure Vessels Piping 2005;82:860–71.
[8] Long RS, Liu WJ, Xing F, Wang HB. Numerical simulation of thermal behavior during laser metal deposition shaping. Trans Nonferrous Met Soc China 2008;18:691–9.
[9] Deng D, Murakawa H. Numerical simulation of temperature field and residual stress in multi-pass welds in stainless steel pipe and comparison with experimental measurements. Comput Mater Sci 2006;37:269–77.
[10] Jia W, Tong H, He W, Lin X, Huang W. Numerical microstructure simulation of laser rapid forming 316L stainless steel. Acta Metall Sin (China) 2010;46(2):135–40.
[11] Kattamis TZ, Coughlin JC, Flemings MC. Trans Metall Soc – AIME 1967;239:1504.
[12] Majumdar Jyotsna Dutta, Li Lin. Studies on direct laser cladding of SiC dispersed AISI 316L stainless steel. Metall Mater Trans A: Phys Metall Mater Sci 2009;40(12):3001–8.
[13] Boisselier Didier, Sankaré Simon. Influence of powder characteristics in laser direct metal deposition of ss316l for metallic parts manufacturing. Phys Proc 2012;39:455–63.
[14] Dutta Majumdar J, Pinkerton A, Liu Z, Manna I, Li L. Mechanical and electrochemical properties of multiple-layer diode laser cladding of 316L stainless steel. Appl Surf Sci 2005;247:373–7.
[15] Neela V, De A. Three-dimensional heat transfer analysis of LENSTM process using finite element method. International Journal of Advanced Manufacturing Technology 2009;45:935–43.
[16] Dutta Majumdar J, Pinkerton A, Liu Z, Manna I, Li L. Microstructure characterisation and process optimization of laser assisted rapid manufacturing of 316L stainless steel. Appl Surf Sci 2005;247:320–7.